Comparative investigation of the fatigue limit of additive-manufactured and rolled 316 steel based on self-heating approach

Yinfeng Cao, Ziad Moumni, Jihong Zhu, Yahui Zhang, Yajun You, Weihong Zhang

Comparative investigation of the fatigue limit of additive-manufactured and rolled 316 steel based on self-heating approach

Yinfeng Cao[a], Ziad Moumni[a,b,*], Jihong Zhu[a,c,*], Yahui Zhang[a], Yajun You[a], Weihong Zhang[a]

[a] *State IJR Center of Aerospace Design and Additive Manufacturing, Northwestern Polytechnical University, 710072 Xi'an, China*
[b] *IMSIA, CNRS, EDF,CEA,ENSTA-Paris Institut Polytechnique de Paris, 91120 Palaiseau, France*
[c] *MIIT Lab of Metal Additive Manufacturing and Innovative Design, Northwestern Polytechnical University, 710072 Xi'an, China*

Abstract

In this paper, fatigue properties of additive-manufactured (AM) 316 steel are investigated by the rapid fatigue limit evaluation method based on self-heating experiments. To this end, a series of tensile cycling experiments are carried out on AM 316 steel specimens; temperature variation resulting from the self-heating phenomenon is recorded by an infrared thermography (IR) camera and fatigue limit is deduced. To compare with the properties of traditionally processed materials, the fatigue limit of rolled 316 steel is also investigated using the same procedure. The experimental results show that the AM 316 steel has a higher fatigue limit than rolled one. In order to interpret this result, microstructures of AM and rolled 316 steel are characterized by metallurgical microscope and X-ray diffractometer (XRD). Furthermore, a crystal-plasticity-fatigue-based model is developed and cyclic

*Corresponding author.
Email addresses: ziad.moumni@ensta.fr (Ziad Moumni), jh.zhu@nwpu.edu.cn (Jihong Zhu)

simulations are carried out. The difference of fatigue limit between AM and rolled 316 steel is discussed experimentally and numerically from microscopic viewpoint, including grain size and dislocation density. It is shown that : 1) the AM process induces coarsening of the grains and reduction of ductility, and 2) ductility plays a much important role than refining grain size on fatigue limit. For this reason, AM 316 steel presents a higher fatigue limit than 316 rolled steel.
Keywords: Fatigue, additive manufacturing, 316 steel, self-heating, XRD, crystal plasticity.

---

1. Introduction

In recent years, additive manufacturing (AM) technology has been utilized to generate functional parts rapidly, which provides an opportunity to manufacture complex-shaped, functionally graded or custom-tailored parts (Herzog et al., 2016). In the fields of aerospace, power and energy, AM parts often suffer cyclic loads. Due to the complex thermomechanical solicitations inherent to the AM process, mechanical properties (especially fatigue properties) of AM parts are different from those of conventionally manufactured parts (Bagherifard et al., 2018; Averyanova et al., 2011; Wegener et al., 2013). This motivates the need for investigating their fatigue properties in order to highlight the impact of the process on the fatigue lifetime. To this end, many works have been carried out in the last few years. Riemer et al. (2014) and Martukanitz et al. (2014) proposed to establish the process-microstructure-properties relationships for AM parts in order to predict their fatigue properties in function of the process parameters. Brandl et al. (2012) studied the microstructure, fatigue properties and fracture behavior of AM AlSi10Mg samples and discussed the factors which

effect the fatigue performance. Yadollahi and Shamsaei (2017) compared the fatigue behavior and failure mechanisms of AM metallic part with conventionally manufactured one. They found that the post-manufacturing treatment can improve the fatigue behavior. Yadollahi et al. (2017) studied the effects of building orientation and post-fabrication heat treatment on the fatigue behavior of AM stainless steel. They found that the defects formed during fabrication and building orientation play a significant role on fatigue behavior. Riemer et al. (2014) studied the fatigue performance of stainless steel 316L manufactured by selective laser melting. They analyzed the microstructure and considered the process-microstructure-properties relationships. Pace et al. (2017) studied the microstructural evolution of 316L steel manufactured by Selective Laser Melting after experiencing 80000 cycles. Raabe et al. (2005) studied the influence of crystallographic texture on the behavior of a low carbon steel during cup drawing using crystal plasticity finite element method. Ahmadi et al. (2016) studied the mechanical response of selective laser melting processed 316 steel using crystal plasticity. The effect of microstructural properties, including melt pool size, texture and process-induced defects, on the mechanical properties are studied. Guerchais et al. (2014) studied the influence of geometrical defects on the high cycle fatigue behaviour of an electrolytic copper using isotropic elasticity, cubic elasticity and crystal plasticity.

In the aforementioned works, fatigue analysis for AM parts are mostly carried out using conventional fatigue tests based on S-N curve. Luong (1998) and Rosa and Risitano (2000) proposed a new method to determine the fatigue limit by considering the intrinsic dissipation as fatigue indicator. The intrinsic dissipation is measured thanks to thermographic analysis. De Finis et al. (2015) and Shiozawa et al. (2016) proposed improved rapid

estimation of fatigue limit based on thermographic method to reduce the temperature change caused by the fatigue testing machine itself. The rapid estimation of fatigue limit based on thermographic method is now widely used in various industrial fields (Prochazka et al., 2017; Ummenhofer and Medgenberg, 2009).

In this work, the fatigue limit evaluation based on thermographic methodology is used to compare the fatigue properties of AM and rolled 316 steel parts. The AM 316 steel is manufactured by Selective Laser Melting (SLM) and the rolled 316 steel is produced by cold rolling. The relationships between the mechanical property, namely fatigue, microstructure and fabrication process are highlighted based on self-heating experimental results, XRD analysis and crystal plasticity simulations.

This paper is organized as follows: Section 2 introduces the experiments in detail: materials, specimens geometry, microstructure, experimental instruments, experimental procedures and a recall of the theoretical basis of the self-heating experiment. In Section 3, the computational model including crystal plasticity theory and mesoscopic fatigue criterion are described. The experimental and simulation results are discussed in Section 4 involving not only the relationship between monotonic properties and microstructure but also the effect of grain size and ductility on fatigue properties. Finally, conclusions are provided in Section 5.

2. Experiments

In this paragraph, the experimental procedure to investigate the fatigue limits of both AM and rolled 316 steel using self-heating approach is detailed.

2.1. Materials and specimen geometry

316 steel manufactured by Selective Laser Melting (SLM) and cold rolling were used in this work. AM 316 steel used in this work was produced by a commercial SLM machine (BLT-S310) with the following process parameters: 280 W of laser power, 40 µm of layer thickness and 1050 mm s^{-1} of scanning speed. The cold-rolled 316 steel was produced by Jiangsu Xingda Steel Tyre Cord Co.Ltd China. The tension specimen used has dimensions according to the international standard for tensile testing of metal-ISO 6892-1: 2009 as shown in Fig. 1. The fatigue specimen has dimensions according to ASTM E 466-2007 as shown in Fig. 2. Before the fatigue experiments, the fatigue specimens of both the AM and rolled 316 steel were polished.

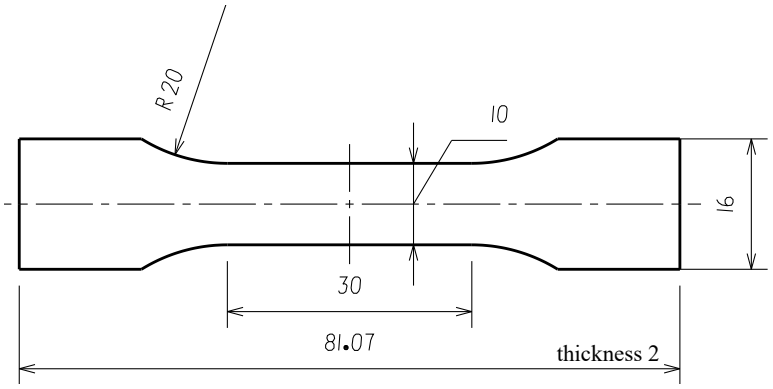

Figure 1: Dimension (mm) and geometry of tension specimens.

2.2. Microstructure characterization and X-ray diffraction analysis

Microstructure characterization was carried out using an Olympus-PMG3 metallographic microscope. Before the microstructure characterization, both the AM 316 steel and rolled 316 steel were subjected to the following metallographic preparation: grinding on SiC papers with granulations of 120, 240, 500, 1200 and 2400, in sequence, polishing with

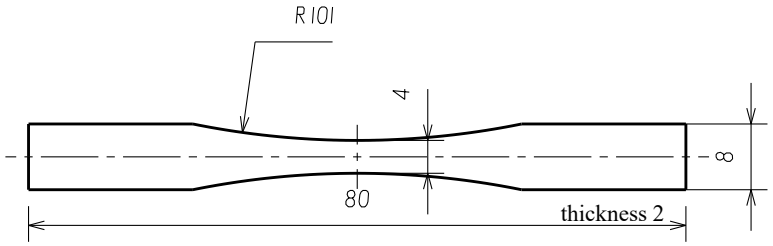

Figure 2: Dimension (mm) and geometry of fatigue specimens.

diamond suspensions (3 µm, 1 µm and 0.25 µm) and polishing with silica suspensions of 0.1 µm and 0.06 µm. $H_2O + HCl + HNO_3$ (1:2:1) was used to etch the specimens. Microstructures of AM 316 steel and rolled 316 steel are shown in Fig. 3. It is shown that the grain of AM 316 steel is much larger than that of rolled 316 steel.

The X-Ray diffraction patterns of both AM and rolled 316 steel are obtained using an X-ray diffractometer (XRD-7000, Shimadzu). As shown in Fig. 4, both AM and rolled 316 steel are composed of austenite phase and ferrite phase. Austenite has a face-centered cubic structure (FCC) and ferrite has a body-centered cubic structure (BCC). Compared with AM 316 steel, rolled 316 steel contains more austenite phase.

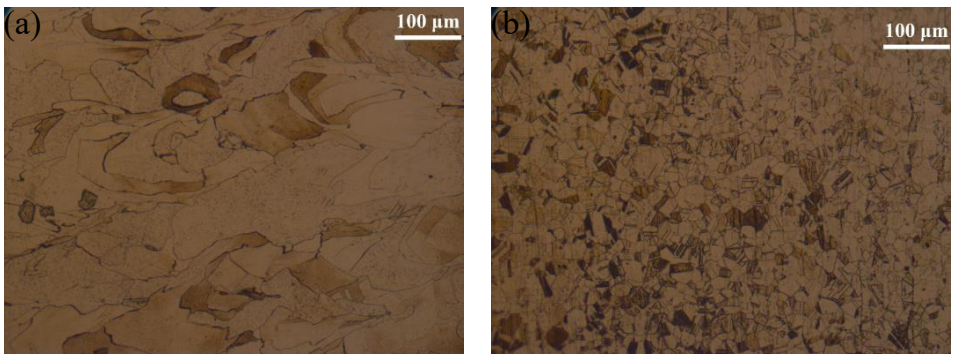

Figure 3: Microstructure of 316 steel: (a) AM 316 steel; (b) rolled 316 steel.

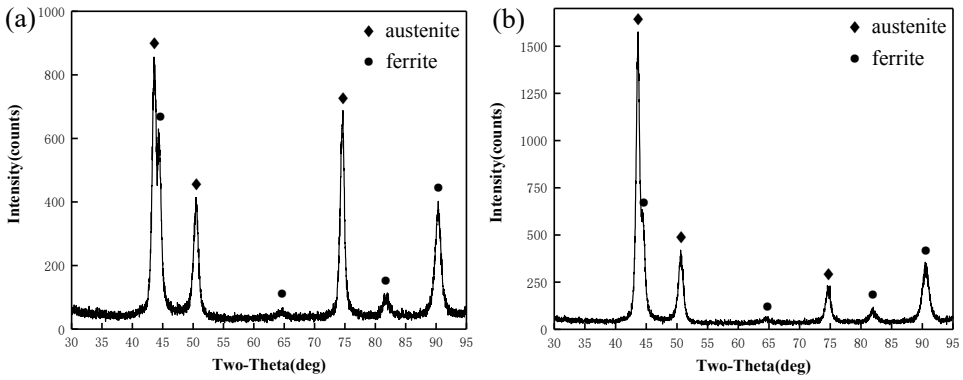

Figure 4: X-ray diffraction patterns of 316 steel: (a) AM 316 steel; (b) rolled 316 steel.

2.3. Instruments and experiment procedures

The tensile tests were carried out at a loading rate of $2\,\mathrm{mm\,min^{-1}}$ using an Instron Testing system with a load capacity of 100 kN. An Epsilon axial extensometer was used to measure the strain. The obtained tensile stress-strain curves of both AM and rolled 316 steel are shown in Fig. 5.

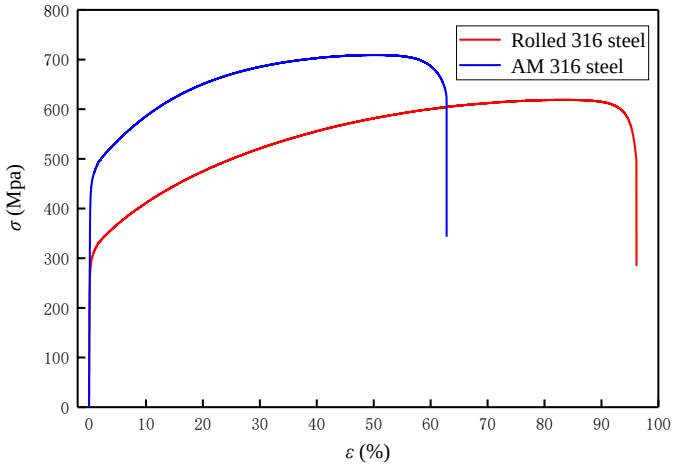

Figure 5: The stress-strain curve of AM 316 steel specimen and rolled 316 steel specimen.

Fatigue tests were carried out using a Bose Electroforce 3510-AT fatigue test machine. Load and displacement signals were captured by Bose Wintest

7 software and processed by a PC. The IR camera Flir SC7700 was used to obtain thermal data on the surface of the specimen. As shown in Fig. 6, the fatigue specimens were coated with a black matte paint to maximize their emissivity and they were enclosed in an insulating box to avoid the heat reflections caused by external heat sources. Meanwhile, a painted unloaded steel plate acting as a black body was used to monitor the environment temperature in the insulating chamber.

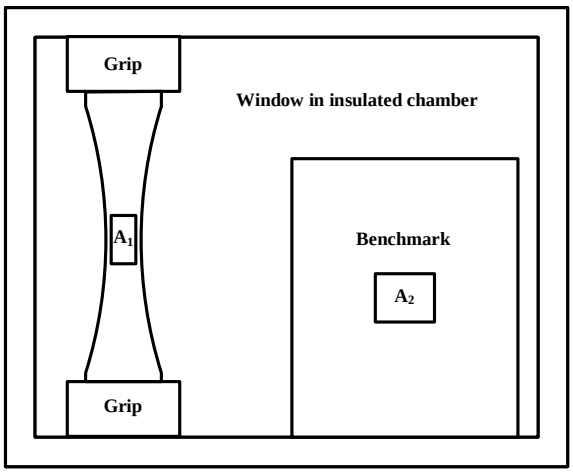

Figure 6: Surface temperature of the specimen and benchmark.

According to the results of tensile tests as shown in Fig. 5, a stepped loading procedure as shown in Table 1 was applied to the specimen with the load characterized by stress ratio $R = 0.1$ and frequency 20 Hz. Each load step lasts 2000 cycles to ensure that the temperature of specimen stabilizes at the end of load step. The IR camera scans with a frequency of 20 frames per second. A typical temperature trend under 2000 loading cycles is shown in Fig. 7.

As shown in Fig. 6, the calculated average temperatures of two rectangular areas are recorded during the test. T_{A_1} and T_{A_2} represent the

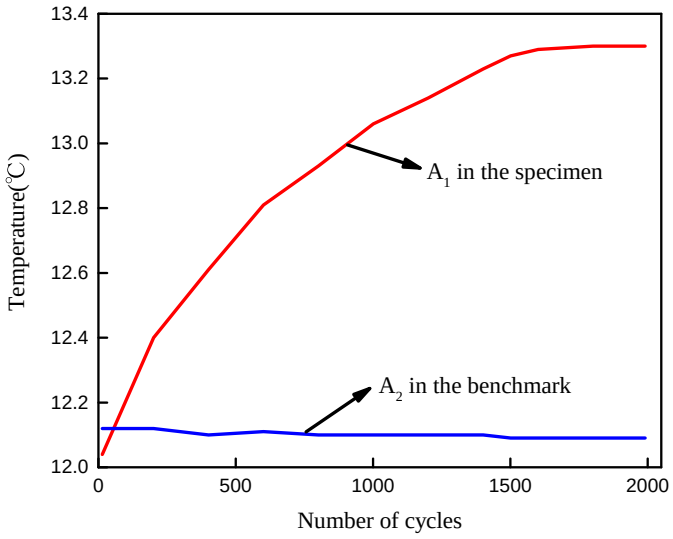

Figure 7: Typical temperature trend under 2000 loading cycles

surface temperature on the region at the middle part of the specimen and at the benchmark, respectively. The temperature variation of the specimen ΔT can be written as

$$\Delta T = (T_{\mathrm{A}_1} - T_{\mathrm{A}_2}) - \min\left(T_{\mathrm{A}_1} - T_{\mathrm{A}_2}\right). \tag{1}$$

After 2000 loading cycles in each load step, ΔT stabilizes. Then the max temperature variation $\Delta T_{\max}$ is used to characterize the dissipated energy. The fatigue limit can be estimated by the relation between $\Delta T_{\max}$ and $\Delta\sigma/2$.

2.4. The theoretical basis of the self-heating approach

The thermal data recorded during the test are analyzed to relate the surface temperature of specimen to its fatigue dissipation. This can be demonstrated using the heat equation given by ((Luong, 1998)):

$$\rho C_v \dot{T} = \rho r + K\Delta^2 T - \left(\boldsymbol{\beta} : \boldsymbol{D} : \dot{\boldsymbol{E}}^e\right) T + \boldsymbol{S} : \boldsymbol{E}^i. \tag{2}$$

Table 1: Loading table in terms of stress (semi-amplitude $\Delta\sigma/2$): the same specimen of rolled 316 steel and AM 316 steel.

Loading step	Rolled 316 steel $\Delta\sigma/2$ (MPa)	AM 316 steel $\Delta\sigma/2$ (MPa)
1	30	100
2	40	110
3	50	120
4	60	130
5	70	140
6	80	150
7	90	160
8	100	170
9	110	180
10	120	190
11	130	200
12	140	210
13	150	220
14	160	230
15	170	240
16	180	250

where ρ is the density, C_v is the specific heat at constant deformation, ρC_v is the volumetric heat capacity of the material, r is the heat supply, K is the thermal conductivity, T is absolute temperature, $\boldsymbol{\beta}$ is a scalar multiplied times the second-order identity tensor, which represents the coefficient of the thermal expansion, $\boldsymbol{D}$ is the fourth-order elasticity tensor, $\boldsymbol{S}$ is the second

Piola-Kirchhoff stress tensor, $\boldsymbol{E}^e$ is the elastic strain tensor and $\boldsymbol{E}^i$ is the inelastic strain tensor. A typical ΔT-stress amplitude diagram is shown in Fig. 8. When the stress amplitude exceeds a threshold, the temperature variation versus the applied stress amplitude curve presents a slope variation (it becomes non derivable), indicating that a new dissipative phenomenon occurs in the specimen. In the low temperature regime (Group 1, 2, 3 and 4) there are no persistent slip bands (PSBs) in the material and the material is elastic at both macroscopic and mesoscopic scales. According to Eq. (2), the temperature variation is mainly due to the thermoelasticity effect $-\left(\boldsymbol{\beta} : \boldsymbol{D} : \dot{\boldsymbol{E}}^e\right) T$. In the high temperature region (Group 5, 6, 7 and 8), PSBs occur in the material. And from Group 5 to Group 8, the number of PSBs increases with the stress amplitude (Munier et al., 2014, 2017). The material is no longer elastic in mesoscopic scale due to the dissipative phenomenon occurring in the interface between PSBs and elasto-plastic matrix. Therefore, the temperature varies significantly due to both thermoelasticity effect $-\left(\boldsymbol{\beta} : \boldsymbol{D} : \dot{\boldsymbol{E}}^e\right) T$ and instrinsic $\boldsymbol{S} : \boldsymbol{E}^i$. According to Luong's method (Luong, 1998; Prochazka et al., 2017), the intersection of curves in the low and high temperature regimes can be seen as the beginning of PSBs initiation and used to estimate the fatigue limit empirically .

3. Computational model

In this paragraph, a computational model based on crystal plasticity theory and a mesoscopic fatigue criterion is established in order to simulate the aforementioned experimentally investigated phenomena, namely the effect of the grain size and the ductility.

To this end, a RVE ($0.25\,\mathrm{mm} \times 0.25\,\mathrm{mm} \times 0.25\,\mathrm{mm}$) shown in Fig. 9 is

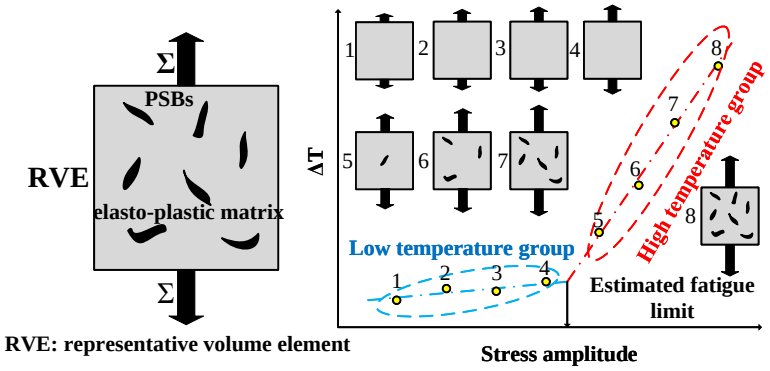

Figure 8: Change of temperature and the fatigue estimation based on temperature.

considered. It is constructed by 125 single crystal grains, which are meshed with eight-node elements and assigned with a set of orientations by random generation. To model the mechanical response of the RVE at the grain level, the crystal plasticity theory is applied using the user-material subroutine (UMAT) developed by (Huang, 1991).

A slip system is denoted (α) and it corresponds to the combination of a slip plane, identified by its normal $\boldsymbol{n}^{(\alpha)}$, and a slip direction, $\boldsymbol{s}^{(\alpha)}$. The rate of crystallographic glide strain $\dot{\gamma}^{(\alpha)}$ only depends on the resolved shear stress $\tau^{(\alpha)}$ (Hill and Rice, 1972)

$$\dot{\gamma}^{(\alpha)} = \dot{a}^{(\alpha)} \left(\frac{\tau^{(\alpha)}}{g^{(\alpha)}} \right) \left| \frac{\tau^{(\alpha)}}{g^{(\alpha)}} \right|^{n-1}. \tag{3}$$

where $\dot{a}^{(\alpha)}$ represents the reference strain rate, $g^{(\alpha)}$ the strength of current slip system and n the strain-rate-sensitivity parameter. The resolved shear stress $\tau^{(\alpha)}$ acting on α can be calculated from the stress tensor $\boldsymbol{\sigma}$ by means of the orientation tensor $\boldsymbol{m}^{(\alpha)}$ (Eq. (4) and Eq. (5)). According to $\boldsymbol{m}^{(\alpha)}$, it is then possible to calculate the plastic strain rate $\dot{\boldsymbol{\epsilon}}^{\mathrm{p}}$ (Eq. (6)).

$$\tau^{(\alpha)} = \boldsymbol{m}^{(\alpha)} : \boldsymbol{\sigma}. \tag{4}$$

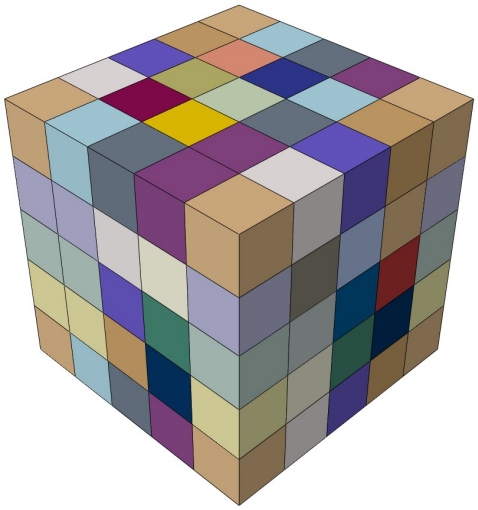

Figure 9: The FE model of the RVE.

$$\boldsymbol{m}^{(\alpha)} = \frac{1}{2}\left(\boldsymbol{n}^{(\alpha)} \otimes \boldsymbol{s}^{(\alpha)} + \boldsymbol{s}^{(\alpha)} \otimes \boldsymbol{n}^{(\alpha)}\right). \tag{5}$$

$$\dot{\boldsymbol{\epsilon}}^{\mathrm{p}} = \sum_{\alpha \text{ active}} \dot{\gamma}^{(\alpha)} \boldsymbol{m}^{(\alpha)}. \tag{6}$$

The evolution of the current strength $g^{(\alpha)}$ can be calculated by the slip hardening modulus $h_{\alpha\beta}$ (Eq. (7)). Here $h_{\alpha\alpha}$ and $h_{\alpha\beta}$ are self and latent hardening moduli, respectively. According to the hardening law proposed by (Peirce et al., 1983), the self and latent hardening moduli can be calculated by the Taylor cumulative shear strain γ on all the slip systems (Eq. (8) and Eq. (9)).

$$\dot{g}^{(\alpha)} = \sum_{\beta} h_{\alpha\beta} \dot{\gamma}^{(\beta)}. \tag{7}$$

$$\begin{aligned} h_{\alpha\alpha} &= h_0 \mathrm{sech}^2\left(\frac{h_0 \gamma}{\tau_s - \tau_0}\right), \\ h_{\alpha\beta} &= q h_{\alpha\alpha} \ (\alpha \neq \beta). \end{aligned} \tag{8}$$

$$\gamma = \sum_{\alpha} \int_0^t \left| \dot{\gamma}^{(\alpha)} \right| \mathrm{d}t. \tag{9}$$

where h_0 and τ_0 are the initial hardening modulus and yield stress which equals the initial value of current strength $g^{(\alpha)}(0)$, respectively. τ_s is the reference stress where large plastic flow initiates and q is a hardening factor.

In order to consider the effect of grain size on the mechanical response, the Hall-Petch relation is introduced here to relate yield stress and grain size

$$\tau_0 = \tau_{\mathrm{R}} + \frac{k_{\mathrm{y}}}{\sqrt{d_{\mathrm{m}}}}. \tag{10}$$

where τ_{R} is the intrinsic hardness of the material. d_m and k_{y} are the average grain size and Hall-Petch coefficient, respectively.

To implement the crystal plasticity model, material parameters for the FCC AISI 316L single crystal (Simonovski et al., 2005) are used. And the Hall-Petch coefficient k_y for FCC metal (Liu et al., 2013) is adopted. All the material parameters are summarized in Table 2.

Table 2: Material parameters used for the 316 steel.

C_{iiii} (MPa)	C_{iijj} (MPa)	C_{ijij} (MPa)	h_0 (MPa)	τ_s (MPa)	τ_R (MPa)	n	q	$\dot{a}^{(\alpha)}$	k_y (MPa µm$^{-0.5}$)
163 680	110 160	100 960	330	270	90	55	1	0.001	600

In order to study the effect of the grain size on the fatigue limit two different grain sizes are considered(60 µm and 120 µm), which, according to the Hall-Petch relation, corresponds to the values of τ_0 167.46 MPa and 144.47 MPa respectively. To consider the effect of ductility on the fatigue limit, two strain-rate-sensitivity parameter are considered $n = 55$ and 10, respectively.

In order to study the effect of the grain size and ductility on the fatigue limit, a fatigue criterion at the mesoscopic (grain scale) based on the concept of elastic shakedown proposed by (Papadopoulos, 1994) is adopted. It assumes that a fatigue crack does not initiate in a grain if the accumulated plastic slip on a given slip system does not exceed a threshold. To this end, the Papadopulos's fatigue criterion is expressed in terms of the mesoscopic quantities instead of the macroscopic quantities as:

$$\begin{aligned} f &= \frac{1}{b}\sqrt{\langle \tau_{s,\mathrm{a}}^2 \rangle} + \frac{a}{b}\max_t[\langle \sigma_n(t) \rangle] \leq 1, \\ \sqrt{\langle \tau_{s,\mathrm{a}}^2 \rangle} &= \sqrt{5}\sqrt{\frac{1}{N_s}\sum_{g=1}^{N_g}\left[\frac{1}{N_g}\sum_{s=1}^{N_s}\tau_{s,a}^2(g,s)\right]}, \\ \langle \sigma_n(t) \rangle &= \frac{1}{N_p}\sum_{g=1}^{N_g}\left[\frac{1}{N_g}\sum_{p=1}^{N_p}\sigma_n(g,p,t)\right]. \end{aligned} \tag{11}$$

where $\tau_{s,a}$ is the mesoscopic resolved shear stress amplitude along every slip systems in the polycrystal. σ_n is the mesoscopic normal stress along every slip planes in the polycrystal. N_s and N_p are the number of slip systems and slip planes in one grain, respectively. N_g is the number of grains in the polycrystal and f is the fatigue factor. a and b are material parameters, which can be calculated in function of fatigue limits relative to fully reversed bending f_{-1} and fully reversed torsion t_{-1}. $\sqrt{\langle \tau_{s,\mathrm{a}}^2 \rangle}$ is the mean value of the resolved shear stress along every slip system in the polycrystal corresponding to Mises norm. $\langle \sigma_n(t) \rangle$ is the mean value of the normal stress acting on these planes corresponding to the hydrostatic tension. In this paper, the values $t_{-1} = 196.2\,\mathrm{MPa}$ and $f_{-1} = 313.9\,\mathrm{MPa}$ in (Papadopoulos, 1994) are adopted.

4. Results and discussion

4.1. Monotonic properties

The stress-strain curves of both AM and rolled 316 steel in Fig. 5 clearly show that both yield stress (YS) and ultimate tensile stress (UTS) of rolled 316 steel are lower than those of AM 316 steel, while rolled 316 steel presents a higher ductility. Furthermore fractographic analysis, using a scanning electron microscope (SEM, VEGA3 TESCAN), shown in Fig. 10 also reveals that the rolled 316 steel has a higher ductility. In fact, smaller and shallower dimples can be observed in the fracture surface of AM 316 steel compared with rolled one. Indeed, bigger and deeper plastic dimples can accommodate larger strain during the tension (Xu et al., 2014).

In addition, XRD analysis shown in Fig. 4 confirms this results since rolled 316 steel contains more austenite phase (FCC) and less ferrite phase (BCC). In fact, as reported in (Mlikota and Schmauder, 2018) ferrite phase (BCC) has a much higher strength than austenite phase (FCC), while austenite phase has a higher ductility than ferrite phase.

4.2. Fatigue properties

The temperature amplitudes for different stress amplitudes of AM 316 steel specimen and rolled 316 steel specimen are recorded by the IR camera. For the sake of the repeatably, each experiment has been carried out three times. Results relative to AM 316 steel specimen and rolled 316 steel specimen are given in Fig. 11 and Fig. 12, respectively. It is shown that the error related to the estimated fatigue limits measured for the three specimens is very small ($\leq 3\%$) for both AM 316 steel and rolled 316 steel. The fatigue limit of AM 316 steel is about 188 MPa which is larger than that of rolled one (138 MPa). Results are summarized in Table 3.

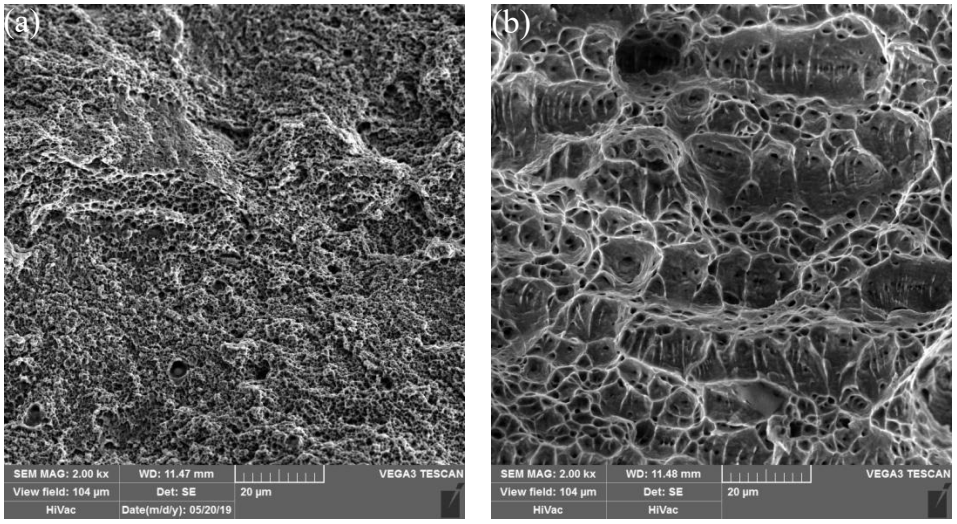

Figure 10: Fractographic analysis of 316 steel: (a) AM 316 steel; (b) rolled 316 steel.

Table 3: Fatigue results based on self-heating method: the fatigue limit σ_L.

Material	σ_L (MPa)			
	Specimen 1	Specimen 2	Specimen 3	Average
Rolled 316 steel	135.99	139.22	137.64	137.62
AM 316 steel	189.03	187.44	188.88	188.45

Results show that the SLM process produce parts with larger fatigue limit compared with traditional manufacturing.

It is well know that dislocations are potential source for fatigue crack initiation. On the other hand, grain boundary plays the role of fatigue crack initiation inhibitor because it induces dislocations pile-ups. Furthermore, small grain presents bigger surface area to volume ratio, which results in larger number of grain boundaries. Therefore, refining grain can inhibit

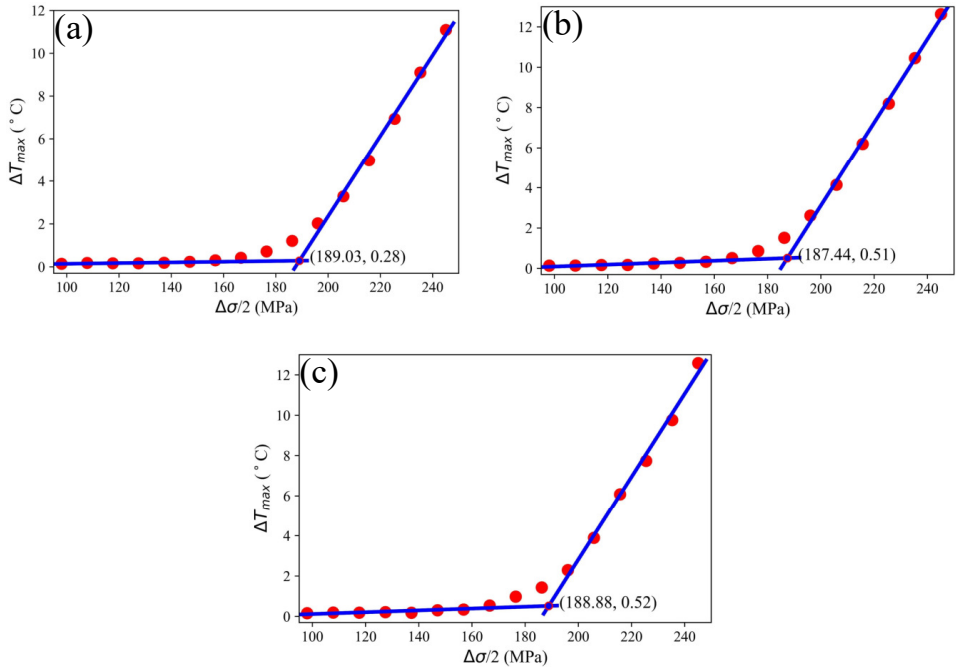

Figure 11: Fatigue limit evaluation of AM 316 steel specimens using Luong's method: (a) specimen 1; (b) specimen 2; (c) specimen 3.

crack initiation and improve the fatigue limit (Ni et al., 2009). As shown in Fig. 3, rolled 316 steel has smaller grains than AM one, resulting in larger fatigue limit of rolled 316 steel than AM one. It is in contradiction with the obtained results, which suggests that other factors influence the fatigue limit such as ductility.

Generally, austenite phase (FCC) has a higher dislocation density than ferrite phase (BCC) (Wroński et al., 2012). And FCC metals are ductile and most BCC metals are semi-brittle (Suresh, 1998). For the ductile metals, dislocations at the interface between the PSB and matrix are the main reason for fatigue crack nucleation (Suresh, 1998). This is because the interface between the PSBs and matrix is a plane of discontinuity across which there

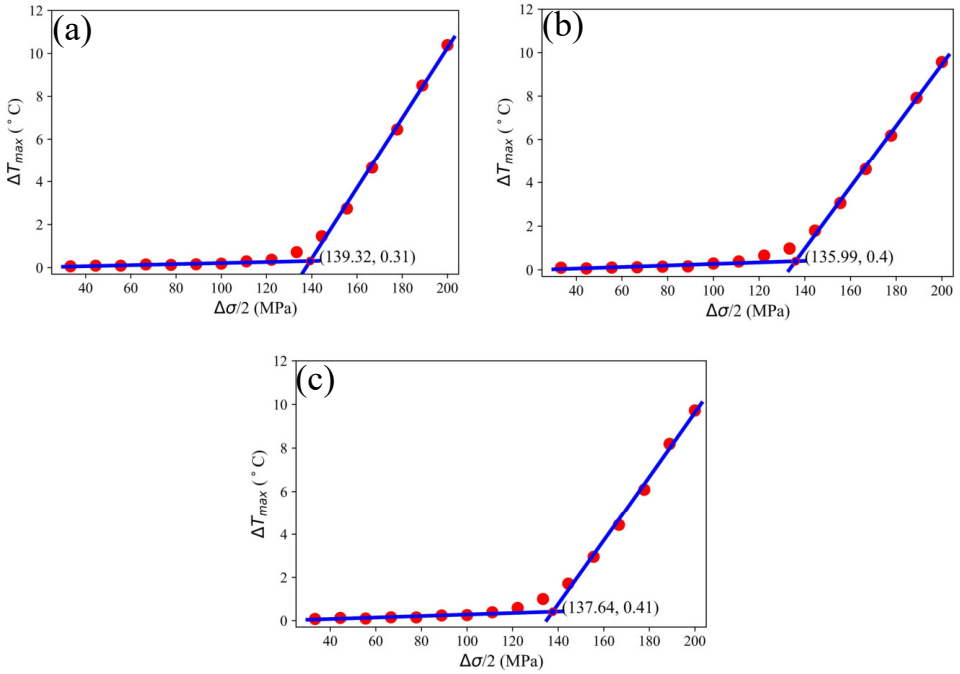

Figure 12: Fatigue limit evaluation of rolled 316 steel specimens using Luong's method: (a) specimen 1; (b) specimen 2; (c) specimen 3.

are abrupt gradients in the density and dislocations distributions. Due to the lower strength of austenite phase, PSBs are much easier formed in the austenite phase than ferrite phase (Wu et al., 2017). According to XRD results, rolled 316 steel contains more austenite phase (FCC) than AM 316 steel. Consequently much more PSBs are formed in rolled 316 steel compared with AM 316 steel as shown in Fig. 13, resulting in a larger number of PSB-matrix interfaces for the same volume. Therefore, rolled 316 steel presents higher probability for fatigue crack nucleation which leads to a smaller fatigue limit.

Hence, high ductility and small grain size present antagonist effect on the fatigue limit. According to the experimental results, the effect of the

ductility plays a more important role on fatigue limit than the grain size.

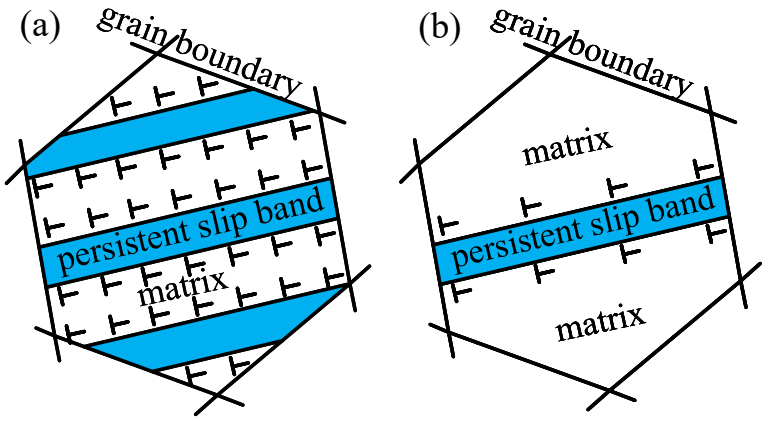

Figure 13: Diagram of dislocations at the interface between PSBs and matrix in the grain: (a) rolled 316 steel; (b) AM 316 steel.

4.3. Simulation results

In this section, the crystal plasticity simulations using the computational model presented above in Section 4.2 aim to verify two issues: first, the fact that grain refinement improves the fatigue limit; second, the fact that reduction of ductility improves the fatigue limit. In the first simulation, the ductility is kept invariant and the grain size changed in order to confirm that grain refinement improves the fatigue limit. And in the second simulation, the grain size is kept invariant and the ductility changed to confirm that reduction of ductility improves the fatigue limit.

For two different average grain sizes considered, 60 µm and 120 µm, Eq. (10) gives τ_0 167.46 MPa and 144.47 MPa, respectively. Applying a macroscopic stress $\Sigma_{11} = 400$ MPa on the RVE using periodic boundary condition (PBC), the obtained equivalent stress-strain curve is shown in Fig. 14. Then a cyclic macroscopic stress $\Sigma_{11}(t)$ ($\Sigma_{11,a} = 200$ MPa and

$R = 0$) is applied during 10 cycles on the RVE and the Papadopuloss fatigue criterion is used to calculated the fatigue factor f. The obtained fatigue factor f equals 0.676 with 60 µm grain size which is smaller than 0.717 obtained with 120 µm grain size. As shown in Eq. (11), smaller f indicates a larger fatigue limit. Therefore, the simulation results also verifies that grain refinement improve the fatigue limit as mentioned in Section 4.2.

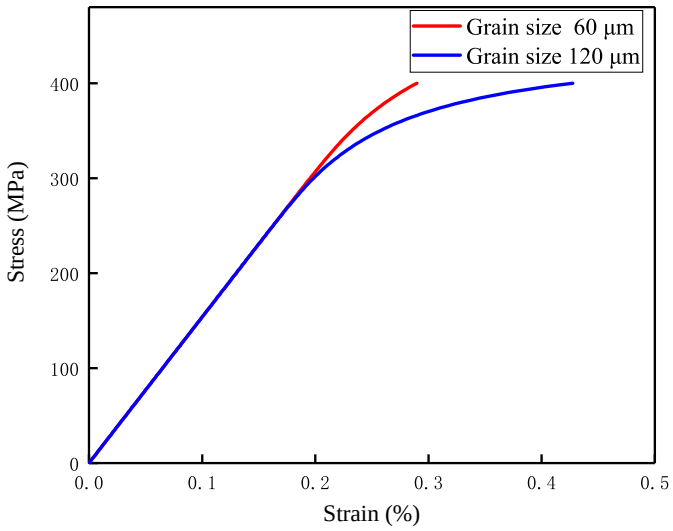

Figure 14: The stress-strain curves under different grain sizes.

The effect of ductility on the fatigue limit is studied by changing the strain-rate-sensitivity parameter n. For $n = 10$ and $n = 55$, the same macroscopic stress Σ_{11} is applied on the RVE, and the stress-strain curves obtained are shown in Fig. 15; the material having a larger strain-rate-sensitivity parameter n is much more ductile. Then the same cyclic macroscopic stress $\Sigma_{11}(t)$ is applied on the RVE and the fatigue factor f is calculated according to the Papadopuloss fatigue criterion. The fatigue factor n equals 0.695 and 0.717 for $n = 10$ and $n = 55$, respectively. The simulation results also verify that reducing the ductility of the material

improves the fatigue limit as mentioned in Section 4.2.

It's worth noting that the real AM and rolled 316 steel would not fail at 0.3 to 0.45 percent strain. But here we are only interested in the simulation of the tendency. Therefore, the 0.3 to 0.45 percent strain is enough to study the tendency.

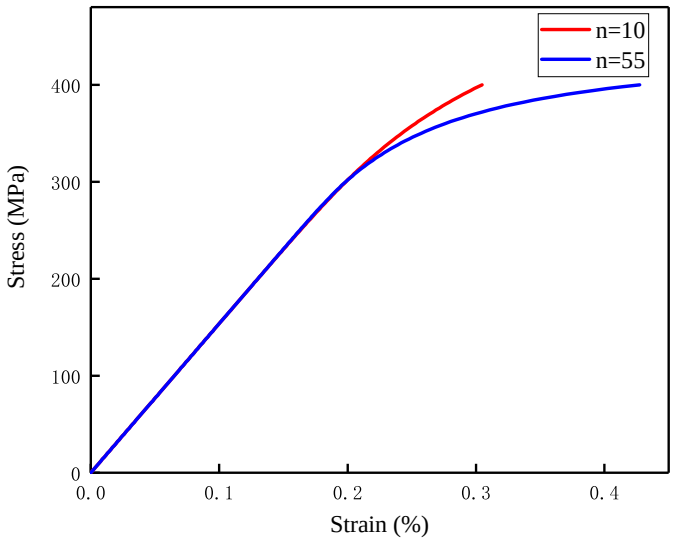

Figure 15: The stress-strain curves under different strain-rate-sensitivity parameters.

5. Conclusions

In this work, fatigue properties of both AM and rolled 316 steel have been investigated and compared using self-heating approach.

To this end, microstructural characterization and X-Ray diffraction measurements have been carried out by metallurgical microscope and X-ray diffractormeter, respectively. Furthermore, a computational model based on crystal plasticity and mesoscopic fatigue criterion has been developed and used to simulate the effect of microstructure, namely grain size and ductility, on the fatigue limit.

It has been shown that ductility plays a more important role than refining grain size on fatigue limit. Due to more austenite phase contained in rolled 316 steel than AM one, rolled 316 steel presents higher ductility and PSBs are easier formed in rolled 316 steel. For this reason, AM 316 steel presents a higher fatigue limit than 316 rolled steel.

6. Acknowledgements

This work is supported by National Key Research and Development Program (2017YFB1102800), NSFC for Excellent Young Scholars (11722219) and Key Project of NSFC (51790171).

Reference

Ahmadi, A., Mirzaeifar, R., Moghaddam, N. S., Turabi, A. S., Karaca, H. E., Elahinia, M., 2016. Effect of manufacturing parameters on mechanical properties of 316l stainless steel parts fabricated by selective laser melting: A computational framework. Materials & Design 112, 328–338.

Averyanova, M., Bertrand, P., Verquin, B., 2011. Studying the influence of initial powder characteristics on the properties of final parts manufactured by the selective laser melting technology. Virtual Physical Prototyping 6 (4), 9.

Bagherifard, S., Beretta, N., Monti, S., Riccio, M., Bandini, M., Guagliano, M., 2018. On the fatigue strength enhancement of additive manufactured alsi10mg parts by mechanical and thermal post-processing. Materials Design 145, 28–41.

Brandl, E., Heckenberger, U., Holzinger, V., Buchbinder, D., 2012. Additive manufactured alsi10mg samples using selective laser melting (slm): Microstructure, high cycle fatigue, and fracture behavior. Materials Design 34 (none), 159–169.

De Finis, R., Palumbo, D., Ancona, F., Galietti, U., 2015. Fatigue limit evaluation of various martensitic stainless steels with new robust thermographic data analysis. International Journal of Fatigue 74, 88–96.

Guerchais, R., Saintier, N., Morel, F., Robert, C., 2014. Micromechanical investigation of the influence of defects in high cycle fatigue. International Journal of Fatigue 67, 159–172.

Herzog, D., Seyda, V., Wycisk, E., Emmelmann, C., 2016. Additive manufacturing of metals. Acta Materialia 117, 371–392.

Hill, R., Rice, J., 1972. Constitutive analysis of elastic-plastic crystals at arbitrary strain. Journal of the Mechanics and Physics of Solids 20 (6), 401–413.

Huang, Y., 1991. A user-material subroutine incroporating single crystal plasticity in the ABAQUS finite element program. Harvard Univ.

Liu, W., Wu, Y., He, J., Nieh, T., Lu, Z., 2013. Grain growth and the hall–petch relationship in a high-entropy fecrnicomn alloy. Scripta Materialia 68 (7), 526–529.

Luong, M. P., 1998. Fatigue limit evaluation of metals using an infrared thermographic technique. Mechanics of Materials 28 (14), 155–163.

Martukanitz, R., Michaleris, P., Palmer, T., DebRoy, T., Liu, Z.-K., Otis, R., Heo, T. W., Chen, L.-Q., 2014. Toward an integrated computational system for describing the additive manufacturing process for metallic materials. Additive Manufacturing 1, 52–63.

Mlikota, M., Schmauder, S., 2018. On the critical resolved shear stress and its importance in the fatigue performance of steels and other metals with different crystallographic structures. Metals 8 (11), 883.

Munier, R., Doudard, C., Calloch, S., Weber, B., 2014. Determination of high cycle fatigue properties of a wide range of steel sheet grades from self-heating measurements. International Journal of Fatigue 63 (63), 46–61.

Munier, R., Doudard, C., Calloch, S., Weber, B., 2017. Identification of the micro-plasticity mechanisms at the origin of self-heating under cyclic loading with low stress amplitude. International Journal of Fatigue 103, 122–135.

Ni, D., Wang, D., Feng, A., Yao, G., Ma, Z., 2009. Enhancing the high-cycle

fatigue strength of mg–9al–1zn casting by friction stir processing. Scripta Materialia 61 (6), 568–571.

Pace, M. L., Guarnaccio, A., Dolce, P., Mollica, D., Parisi, G. P., Lettino, A., Medici, L., Summa, V., Ciancio, R., Santagata, A., 2017. 3d additive manufactured 316l components microstructural features and changes induced by working life cycles. Applied Surface Science 418, S0169433217303458.

Papadopoulos, I. V., 1994. A new criterion of fatigue strength for out-of-phase bending and torsion of hard metals. International Journal of Fatigue 16 (6), 377–384.

Peirce, D., Asaro, R. J., Needleman, A., 1983. Material rate dependence and localized deformation in crystalline solids. Acta metallurgica 31 (12), 1951–1976.

Prochazka, R., Dzugan, J., Konopik, P., 2017. Fatigue limit evaluation of structure materials based on thermographic analysis. Procedia Structural Integrity 7, 315–320.

Raabe, D., Wang, Y., Roters, F., 2005. Crystal plasticity simulation study on the influence of texture on earing in steel. Computational Materials Science 34 (3), 221–234.

Riemer, A., Leuders, S., Thne, M., Richard, H. A., Trster, T., Niendorf, T., 2014. On the fatigue crack growth behavior in 316l stainless steel manufactured by selective laser melting. Engineering Fracture Mechanics 120 (4), 15–25.

Rosa, G. L., Risitano, A., 2000. Thermographic methodology for rapid determination of the fatigue limit of materials and mechanical components . International Journal of Fatigue 22 (1), 65–73.

Shiozawa, D., Inagawa, T., Washio, T., Sakagami, T., 2016. Fatigue limit estimation of stainless steels with new dissipated energy data analysis. Procedia Structural Integrity 2, 2091–2096.

Simonovski, I., Nilsson, K.-F., Cizelj, L., 2005. Material properties calibration for 316 l steel using polycrystalline model. In: The 13th international conference on nuclear engineering abstracts.

Suresh, S., 1998. Fatigue of materials. Cambridge university press.

Ummenhofer, T., Medgenberg, J., 2009. On the use of infrared thermography for the analysis of fatigue damage processes in welded joints. International Journal of Fatigue 31 (1), 130–137.

Wegener, K., Spierings, A. B., Starr, T. L., 2013. Fatigue performance of additive manufactured metallic parts. Rapid Prototyping Journal 19 (2), 88–94.

Wroński, S., Tarasiuk, J., Bacroix, B., Baczmański, A., Braham, C., 2012. Investigation of plastic deformation heterogeneities in duplex steel by ebsd. Materials Characterization 73, 52–60.

Wu, H. C., Yang, B., Chen, Y. F., Chen, X. D., 2017. Effect of oxidation on the fatigue crack propagation behavior of z3cn20.09m duplex stainless steel in high temperature water. Nuclear Engineering Technology 49 (4), S1738573317300438.

Xu, D., Zu, T., Yin, M., Xu, Y., Han, E., 2014. Mechanical properties of the icosahedral phase reinforced duplex mg–li alloy both at room and elevated temperatures. Journal of Alloys and Compounds 582, 161–166.

Yadollahi, A., Shamsaei, N., 2017. Additive manufacturing of fatigue resistant materials: Challenges and opportunities. International Journal of Fatigue 98 (Complete), 14–31.

Yadollahi, A., Shamsaei, N., Thompson, S. M., Elwany, A., Bian, L., 2017. Effects of building orientation and heat treatment on fatigue behavior of selective laser melted 17-4 ph stainless steel. International Journal of Fatigue 94, 218–235.